Electronic Supporting Information (ESI)

A Wafer-scale Fabrication Method for Three-Dimensional Plasmonic Hollow Nanopillars

D. Jonker[*1#], Z. Jafari[2#], J.P. Winczewski[1], C. Eyovge[1], J. G. E. Gardeniers[1], I. De Leon[*2], A. Susarrey-Arce[*1]

[1]Mesoscale Chemical Systems, MESA+ Institute, University of Twente, PO. Box 217, Enschede 7500AE, The Netherlands

[2]School of Engineering and Sciences, Tecnologico de Monterrey, Monterrey, Nuevo Leon 64849, Mexico

[#]These authors contributed equally.

*Corresponding author(s): d.jonker@utwente.nl, ideleon@tec.mx, a.susarreyarce@utwente.nl

Table of content

Section 1 – Morphological, structural, and FDTD analysis

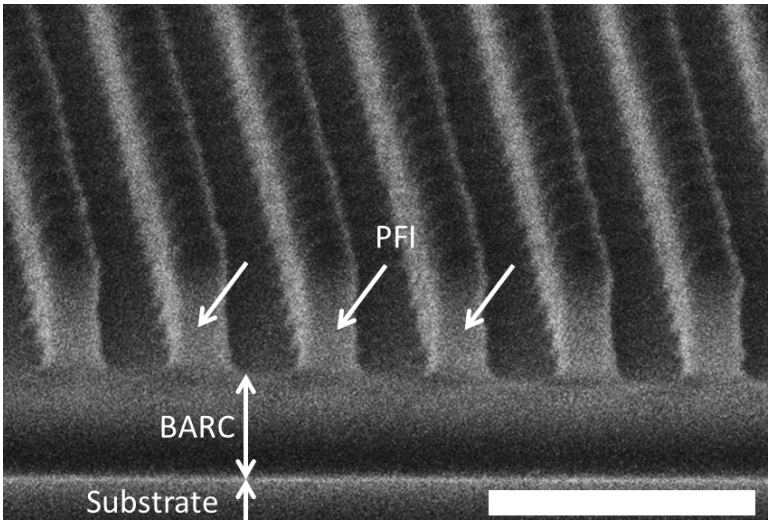

Figure S1. Cross-sectional SEM image of a PFI nanodot array on top of the BARC layer and substrate as obtained by performing oDTL. The scale bar represents 500 nm.

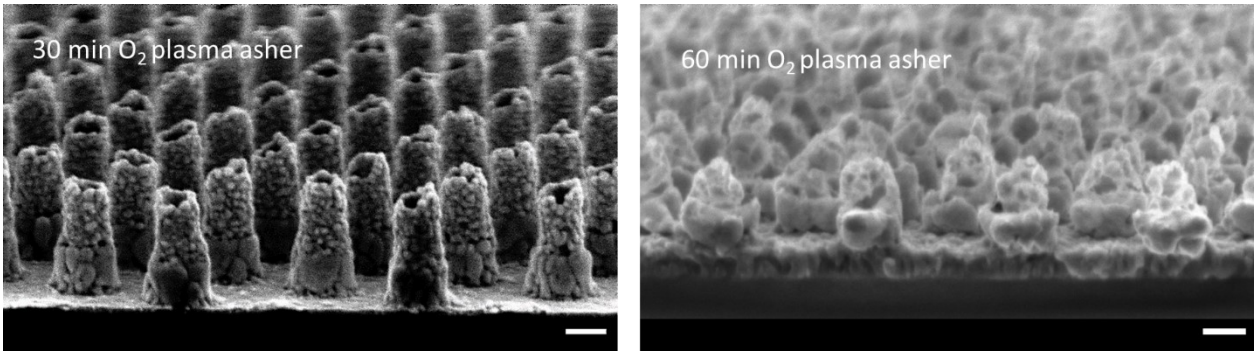

Figure S2. Au-HNP after 30 and 60 min of O_2 plasma treatment in an 800W plasma etcher. The scale bar represents 100 nm

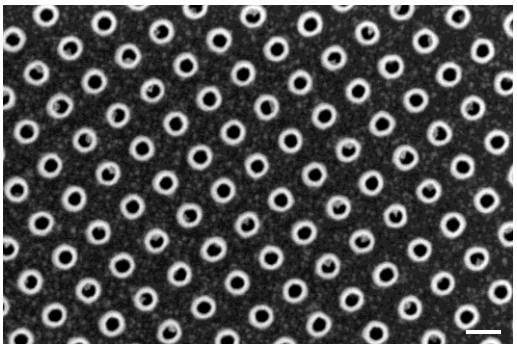

Figure S3. Top-view SEM image of Au-hollow nanopillars after BARC removal in a 25W O_2 plasma for 8 min. The scale bar is set to 200 nm.

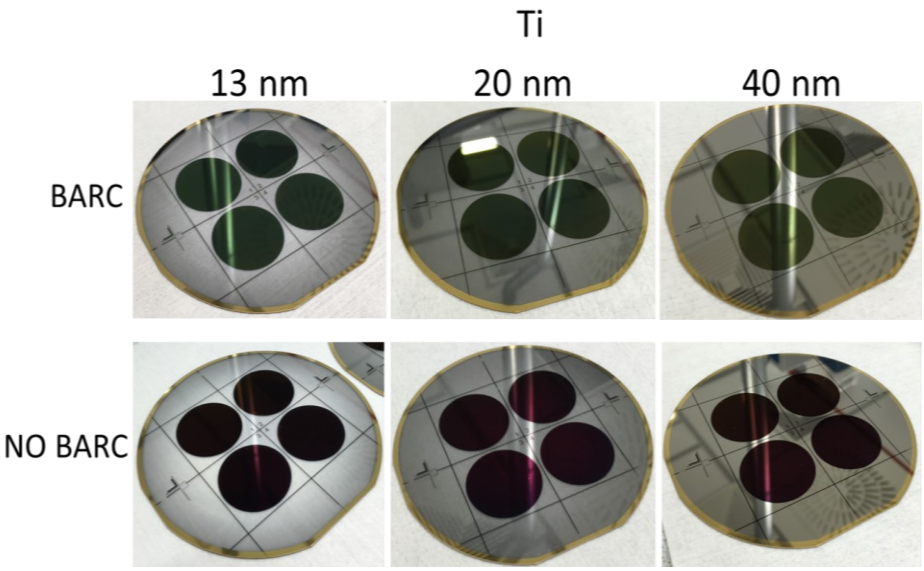

Figure S4 Pictures of SHL patterns over 100 mm MEMpax® substrates, each containing four circular SERS devices of 25mm in diameter, which are divided into 30.3 mm square chips. Dicing lines and alignment markers also consist of the Au-HNP, emphasizing that patterning can be achieved at different macroscopic sizes. An interesting effect is the occurrence of the light strokes, which are visible in each image. These strokes are reflected off a metal duct above the substrates, onto the substrate and back into the camera. Note that they show a difference in color for the different treatments on the substrates. The photographs are taken after IBE, still containing BARC, and after O_2 plasma stripping in an RIE step, yielding the structures without BARC.

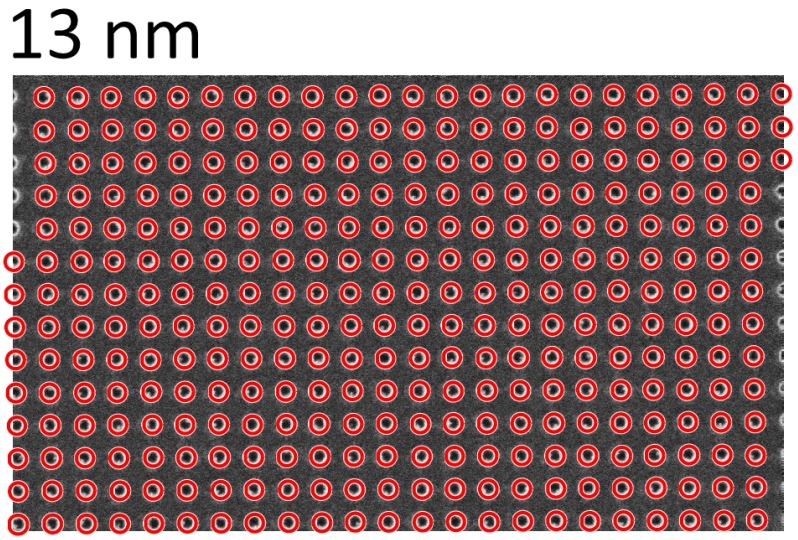

Figure S5. HR-SEM top-view image of AuHNPs. An automated program written in MATLAB analyzes the images indicating the outer base (red) diameters. The measured outer base diameters are shown in **Figure S6**.

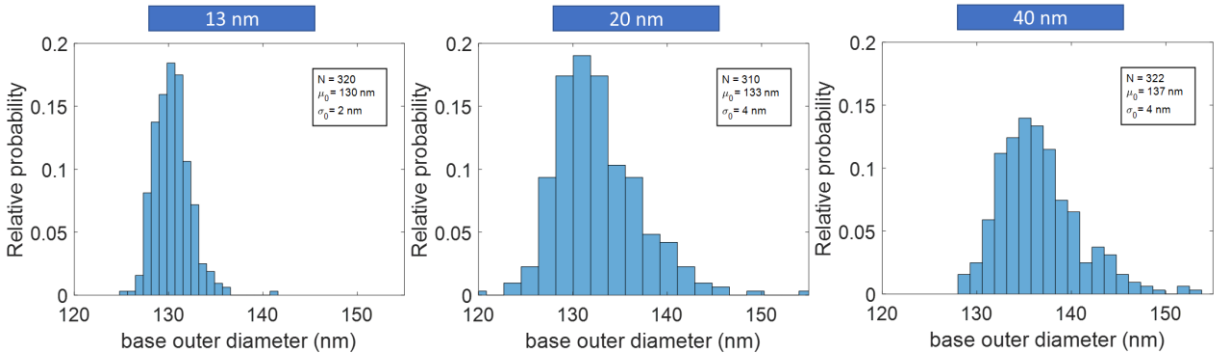

Figure S6. Histogram plots containing the estimated values for the base outer diameters as extracted from the top-view images obtained from the MATLAB code. An example is shown in **Figure S5.** The Sturges formula determines the bin sizes. The μ_0 and σ_0 legends indicate the mean and the standard deviation of the base outer diameter distribution of the Au-HNP structure. N states the number of nanopillars counted.

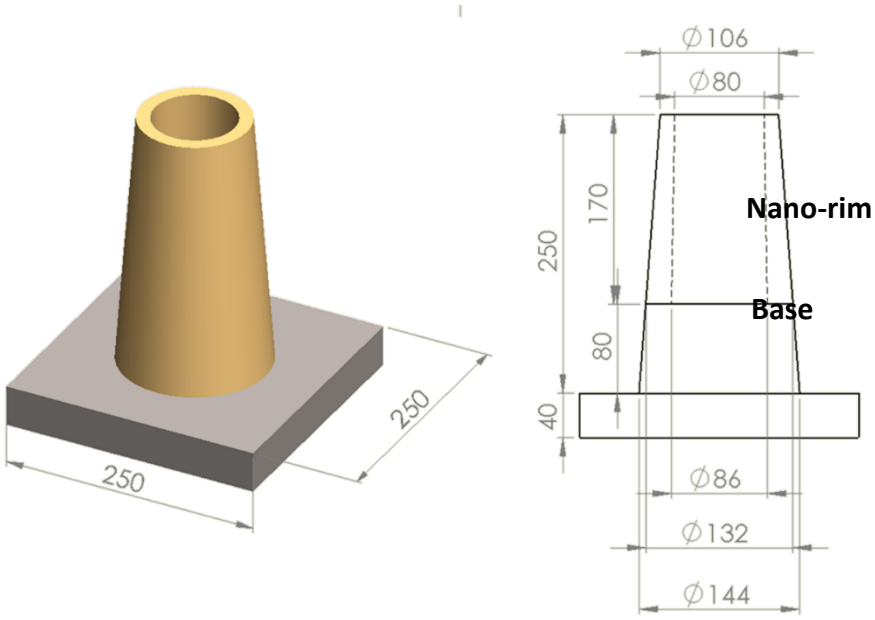

Figure S7. a) schematic representation of a Au-HNP over a titanium layer. b) structural dimensions for Au-HNPs obtained by TEM and SEM analysis. All dimensions are in nm.

The Ti thickness is labeled as 40 nm, but in some experiments it was 13 nm or 20 nm. The Au thickness of the nano-rim varies from 15 ± 3 nm (top) down to 20 nm ± 5 nm (bottom) before reaching the Au-HNP base.

Section 2 - Central composite design

2.1 The factorial design applied to the FDTD results

Factorial design approaches are characterized by the minimization of experimental runs in multivariable studies. In this case, it is assumed that system response is a function of independent variables called factors and noise. In real physical systems, the interaction between factors may further alter the response. Researchers tend to vary factors one-at-a-time in a more traditional approach to characterize the response and optionally tune the process towards an optimized behavior. However, doing so might obscure interactive effects and reduce the probability of finding the right optimal response or observing more complex physical behavior.

Our experiment uses a factorial design approach to create an experimental window based on a central composite design (CCD) for FDTD simulations. The factors considered are the structural dimensions of the Au-HNPs (**Figure S8**) and the thickness of the Ti adhesion layer, which, in turn, are varied over a range broader, but close to those observed in SEM and TEM measurements (**Figure S7**). These structural dimensions are then used to carry out the FDTD simulations, ultimately generating an absorptance spectrum. The numerical optical responses are evaluated, particularly at spectral locations for the dipole mode. After the maximum absorptance is detected, we extract wavelength values. The experimental CCD includes 6 factors, with a total of 53 absorptance spectra, which is the minimum amount of experiments in a CCD with 6 factors, including 5 center point runs. The center-, cube- and star (axial) points are defined in **Figure S8**, together with an illustration containing the parameters.[1,2]

Results are discussed by means of the analysis of variance (ANOVA) and quadratic regression. Performing the ANOVA yields information about the significance of the factors. A backward elimination scheme is performed by iterating the ANOVA and removing terms that fail to meet the significance level. This approach lowers the chance of overfitting by considering the adjusted coefficient of determination, $R^2_{adj,}$ to obtain a R^2_{adj} optimized fit. The regression equation used captures both linear and quadratic responses and linear 2nd order interactions:

$$X_i = a_0 + \sum_{i=1}^{k} a_i x_i + \sum_{i=1}^{k} a_{ii} x_i^2 + \sum_{i<j} \sum a_{ij} x_i x_j + \epsilon \qquad (1)$$

Where x_i is the value of the factor at an experimental setting, $x_i x_j$ represent the 2nd order interactions, and a_i are the corresponding proportionality constants, which are extracted utilizing a least-squares approximation. Lastly, ϵ represents a stochastic error term. Residual

analysis is used to validate the normal distribution of the residuals and the dataset. Note that we do not assume the physical behavior to be of a parabolic behavior, but it allows us to show a form of curvature in the experimental range.

	Inner top(nm)	Outer top(nm)	Inner bottom (nm)	Outer bottom (nm)	Base bottom (nm)	Ti thickness (nm)
Star (low)	65	90	85	120	140	10
Cube (low)	70.8	98.7	89.3	125.8	148.7	24.5
Center (0)	75	105	92.5	130	155	35
Cube (high)	79.2	111.3	95.7	134.2	161.3	45.5
Star (high)	85	120	100	140	170	60

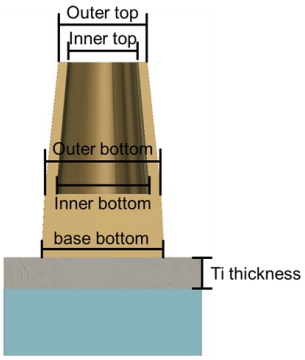

Figure S8 A table containing the definition of the factors varied in the CCD experiment and the absolute values, together with an illustration and indication of the structural parameter accompanying the corresponding factor.

2.2 Input and output data table

The Au-HNPs numerical simulations in **Figure 5d)** of the main text show two absorptance peaks assigned to the dipole and quadrupole modes. The location of these two peaks changes as a function of the input parameters described in **Figure S8**, whereas all individual settings are given in **Table S1**. The dipole peak location and its maximum absorptance for each set of input parameters calculated with FDTD are shown in **Table S2**. In the following, we focus on the dipole mode because this mode is close to the Raman laser lines used in this work, and EFs are larger for this mode.

Table S1. Individual settings were used for the Au-HNP dimensions during CCD FDTD simulations. All dimensions stated are in nanometers.

Run no.	Inner top	Outer top	Inner bottom	Outer bottom	Base bottom	Ti thickness
1	75	105	92.50	130	155	35
2	75	105	92.50	130	155	60
3	70.79	98.69	89.34	125.79	161.30	45.51
4	85	105	92.50	130	155	35
5	75	105	92.50	140	155	35
6	70.79	98.69	95.65	125.79	161.30	24.48
7	75	105	92.50	120	155	35

8	70.79	111.30	89.34	134.20	161.30	45.51
9	79.20	98.69	89.34	134.20	161.30	45.51
10	75	105	92.50	130	155	35
11	79.20	111.30	95.65	134.20	148.69	24.48
12	75	105	92.50	130	155	35
13	79.20	98.69	95.65	125.79	161.30	45.51
14	75	90	92.50	130	155	35
15	75	105	92.50	130	155	35
16	79.20	98.69	89.34	134.20	148.69	24.48
17	75	105	92.50	130	140	35
18	70.79	111.30	95.65	134.20	161.30	24.48
19	70.79	98.69	95.65	134.20	161.30	45.51
20	75	105	92.50	130	170	35
21	79.20	111.30	89.34	125.79	161.30	45.51
22	75	105	92.50	130	155	35
23	70.79	111.30	89.34	125.79	148.69	45.51
24	70.79	111.30	89.34	134.20	148.69	24.48
25	70.79	98.69	95.65	125.79	148.69	45.51
26	70.79	98.69	95.65	134.20	148.69	24.48
27	75	105	92.50	130	155	35
28	79.20	111.30	95.65	125.79	161.30	24.48
29	79.20	111.30	95.65	125.79	148.69	45.51
30	79.20	98.69	95.65	125.79	148.69	24.48
31	70.79	98.69	89.34	134.20	148.69	45.51
32	70.79	111.30	95.65	134.20	148.69	45.51
33	75	120	92.50	130	155	35
34	79.20	111.30	89.34	134.20	161.30	24.48
35	75	105	92.50	130	155	35
36	75	105	92.50	130	155	35
37	79.20	111.30	89.34	134.20	148.69	45.51
38	75	105	92.50	130	155	10
39	65	105	92.50	130	155	35
40	79.20	98.69	95.65	134.20	148.69	45.51
41	75	105	100	130	155	35
42	79.20	98.69	89.34	125.79	148.69	45.51
43	75	105	85	130	155	35

44	70.79	98.69	89.34	125.79	148.69	24.48
45	75	105	92.50	130	155	35
46	70.79	111.30	89.34	125.79	161.30	24.48
47	70.79	98.69	89.34	134.20	161.30	24.48
48	70.79	111.30	95.65	125.79	148.69	24.48
49	79.20	111.30	89.34	125.79	148.69	24.48
50	79.20	98.69	89.34	125.79	161.30	24.48
51	70.79	111.30	95.65	125.79	161.30	45.51
52	79.20	98.69	95.65	134.20	161.30	24.48
53	79.20	111.30	95.65	134.20	161.30	45.51

Table S2. Results for the individual CCD FDTD simulations. The runs marked with * contain values that were extracted manually instead of by a peak detection algorithm. The values marked with – were artificially varied between 0 and 550 nm for the electric dipole peak location, and 0 and 0.5 absorptances, as explained in the text.

Run No.	**Dipole peak(nm)**	**Abs. at Dip.peak**	**Run No.**	**Dipole peak(nm)**	**Abs. at Dip.peak**
1	588	0.64	28	588	0.68
2	588	0.64	29	588	0.649
3	588	0.675	30*	632	0.738
4*	632	0.768	31	584	0.63
5	584	0.617	32	-	-
6	596	0.683	33	-	-
7	596	0.673	34	584	0.645
8	-	-	35	588	0.647
9*	624	0.753	36	588	0.647
10	588	0.647	37	584	0.604
11	584	0.628	38	584	0.7
12	588	0.647	39	-	-
13*	636	0.81	40*	628	0.732
14*	656	0.81	41	592	0.653
15	588	0.647	42*	636	0.766
16*	620	0.7	43	584	0.64
17	588	0.61	44	592	0.654
18	-	-	45	588	0.647

19	588	0.654	46	-	-
20	588	0.678	47	584	0.667
21	584	0.667	48	-	-
22	588	0.647	49	584	0.6495
23	-	-	50	628	0.768
24	-	-	51	-	-
25	592	0.66	52	628	0.745
26	592	0.635	53	588	0.6312
27	588	0.647	-	-	-

2.3 Results and analysis

2.3.1 Empty rows are 0

Analysis of the results in **Table S2** are commenced by performing an ANOVA with a backward elimination scheme at a significance level of 0.05 and polynomial regression. For the missing values in **Table S2** a 0-value was entered for both the electric dipole peak location and maximum absorptance at the peak. The results are first evaluated based on an analysis of the residuals, according to the following equation:

$$r_i = Y_i - X_i \tag{2}$$

Where Y_i is the result extracted from the FDTD simulation and X_i is the result extracted from the derived regression equation (1) at the same settings. When evaluating the residuals by a normal probability plot, as shown in **Figure S9**, it becomes apparent that the residuals do not follow a normal distribution, as indicated by the straight line, and some extreme outliers are presented. Plotting the residuals versus the fitted values indicate that residuals are the largest for the fitted zero values. It is concluded that entering 0 values alters the analysis to such an extent that it becomes impossible to continue the analysis to find anything meaningful.

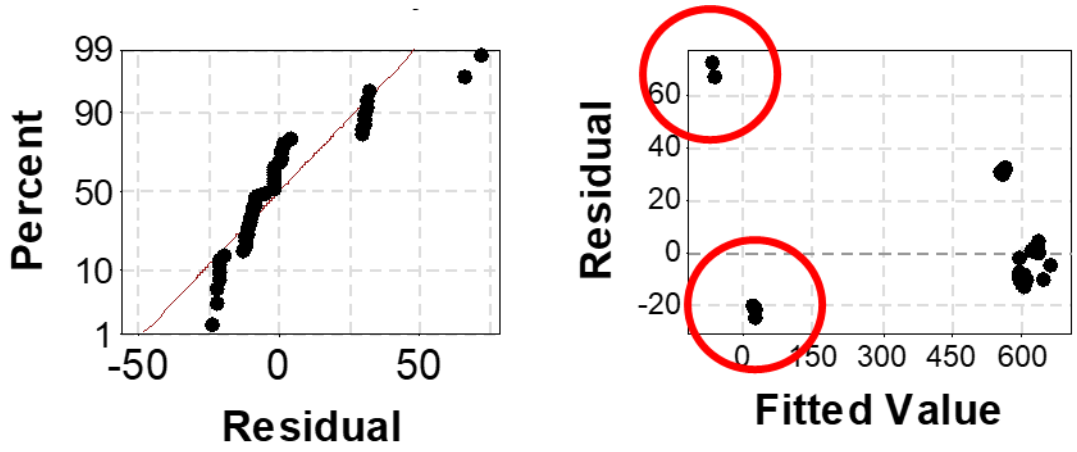

Figure S9. On the left side, a normal probability plot is shown for the residuals where the dots represent the residuals, and the straight line represents a perfectly normal distributed dataset. The right-side contains the residuals plotted for the fitted value extracted from the quadratic regression and calculated proportionality constants, eq. (1)-(2). The red circles show the outliers resulting from entering a 0-value.

2.3.2 Empty rows are λ= 550 nm and A=0.5

The second attempt entails adding in fictive values for the missing data points. Manual inspection of the absorptance spectra revealed that the dipole peak location shifts to shorter wavelengths while also showing a decrease in the peak value in the case of the missing data points, therefore, the choice was made to manually enter estimated values, being 550 nm for dipole peak location and 0.5 for the absorptance maximum. Furthermore, backward elimination is applied at a significance level of α=0.05. Analysis of the results is commenced by first performing an analysis of the residuals, as shown in **Figure S10**. Compared to the 0-value analyses, no extreme outliers are presented.

Next, the results of the regression equation are analyzed by a mean value plot. The results for the factors that have a significant effect on the mean value of the electric dipole mode are shown in **Figure S11**. All structural factors except for the base bottom are found to play a significant role. The largest change for the electric dipole mode absorptance peak is due to a change in the inner and outer top dimensions **Figure S11**. A change in diameter of 20 and 30 nm yields a change in absorptance peak location of ~75 and ~100 nm, respectively. Another interesting observation is the significance of the 2nd order interaction between the inner and outer top diameter **Figure S11**. A larger inner and smaller outer diameter tend to shift the electric dipole mode absorptance location to larger wavelengths.

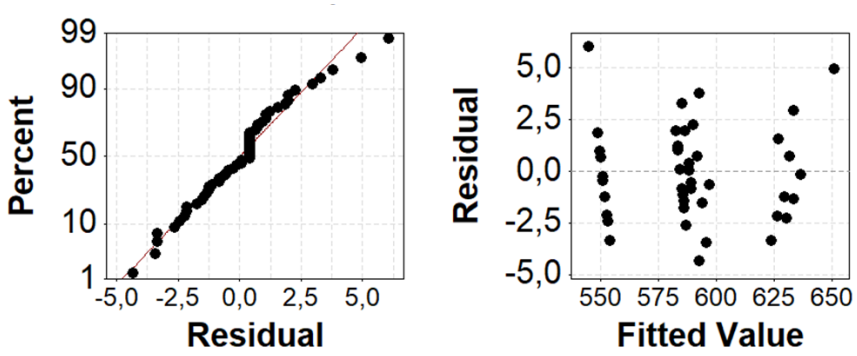

Figure S10 On the left-side, a normal probability plot for the residuals is presented after adding fictive values for the electric dipole peak and a backward elimination scheme. Again, the straight line represents a perfectly normal distributed dataset. b) the residuals versus the fitted values extracted from the regression equation.

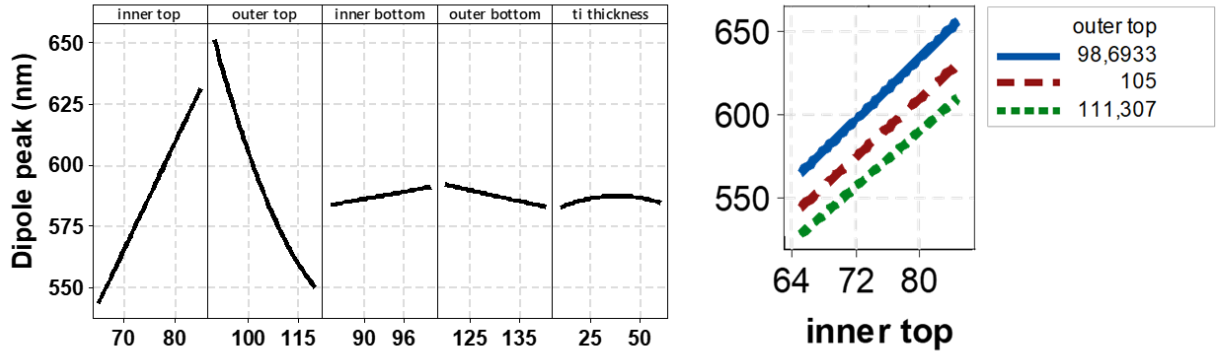

Figure S11 Fitted line plots for the mean value of the electric dipole mode location as a function of the respective structural parameters. All values are in the nm-scale. On the left side, the main factors are plotted while on the right-hand side, the 2nd order interaction between the inner and outer top is shown.

2.3.3 The side-wall thickness

From the analysis performed in **Figures S9 and S10**, the inner- and outer top diameter of the hollow pillar have the largest effect on the electric dipole peak location and absorptance maxima. Considering the interaction, a change in both the inner and outer diameter of the ring structure is also equal to a change in the side-wall thickness of the Au-HNP nano-rim. One can make the difference between the inner and outer top diameters and consider this as a single new variable. This is done in **Figure S12**, where the effect of varying the wall thickness on the absorptance peak location and absorptance peak maxima is shown. It is observed that varying side-wall thickness has a large effect on the optical response.

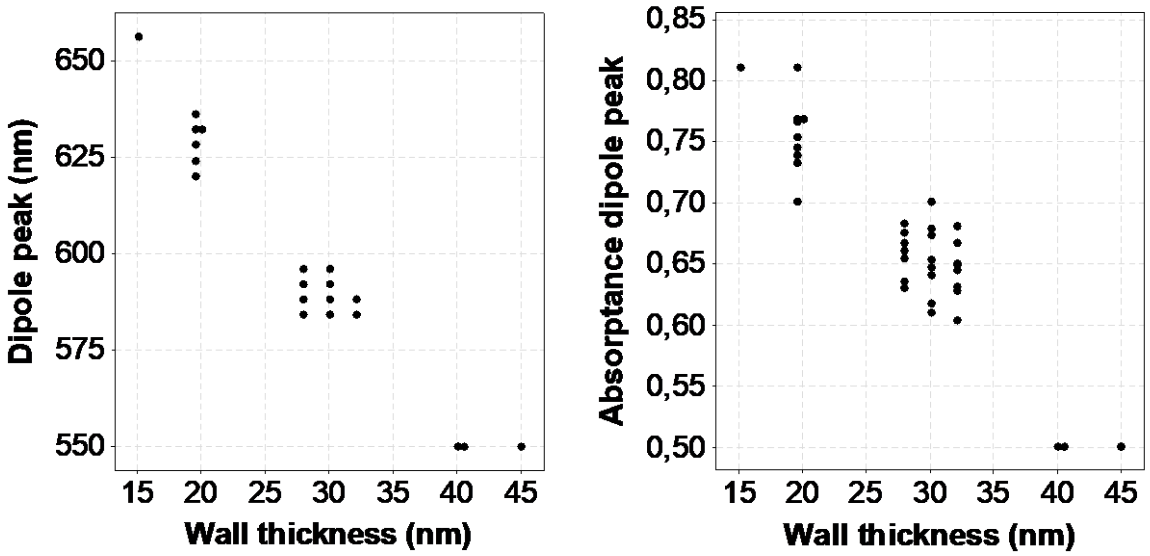

Figure S12 Scatterplots showing the dipole peak locations and absorptance maxima as a function of the nano-rim wall thickness of the Au-HNP structure.

This analysis concludes that the sidewall thickness of the top nano-rim has the dominant effect on the optical response of the dipole mode. It also indicates that the change in the sidewall thickness is the major source of the variations in the measured UV-Vis-NIR spectra. These results are particularly interesting because it can lead to the design of a fabrication experiment in which the sidewall thickness is systematically varied.

Section 3 – Raman enhancement factor of functionalized Au nanopillars

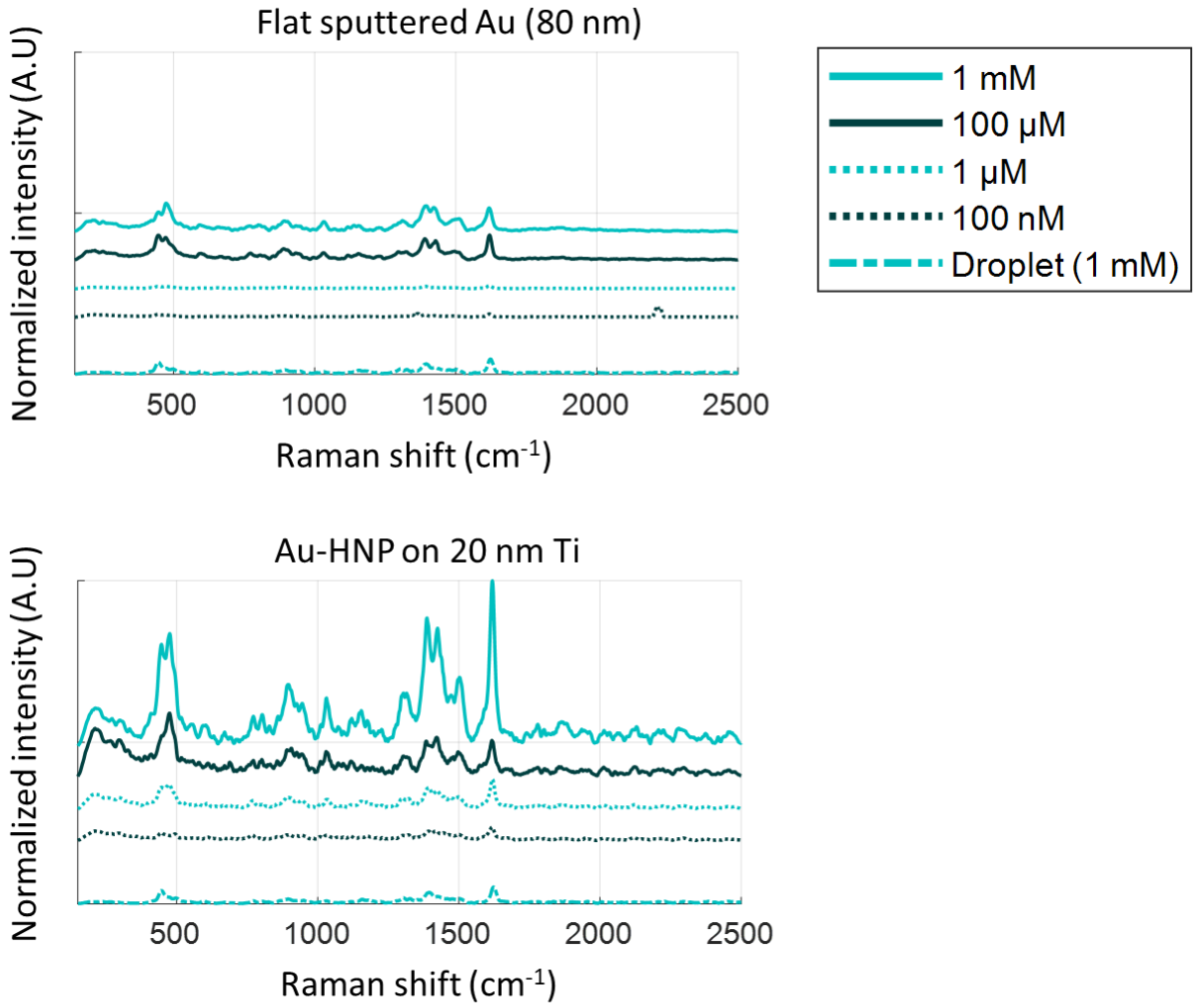

Figure S13 Recorded spectra for a 633 nm excitation laser wavelength at 100x magnification and 0.9 NA. The laser power was 0.5 mW. The spectra were recorded for MB functionalization at different MB concentrations, for a flat sputtered Au reference substrate and an Au-HNP substrate with a 20 nm thick Ti adhesion layer. Measurements are also compared to a measurement on a droplet containing a 1mM concentration of MB. The spectra were normalized for the largest intensity peak and contain an offset to enhance readability.

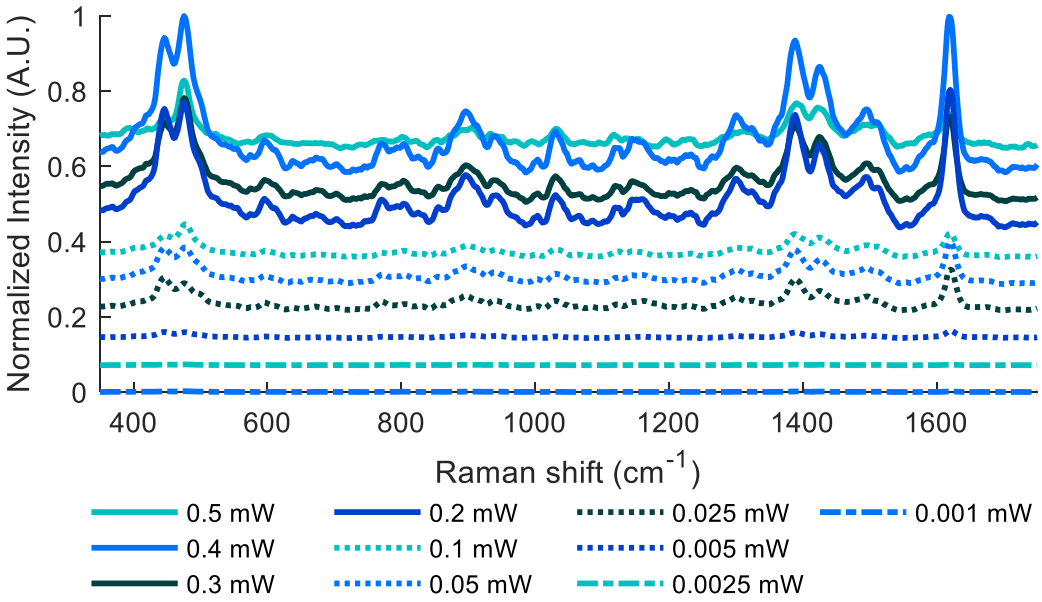

Figure S14 Recorded spectra for a 633 nm excitation laser wavelength at 100x magnification and 0.9 NA. The output laser power was varied between 0.001 mW and 0.5 mW. The spectra were recorded for MB functionalization in a 1mM solution on a Au-HNP substrate with a 20 nm thick Ti adhesion layer. It was observed that for laser powers ≥0.5 mW the measurements were destructive, leaving visible spots on the substrate surface within the measurement integration time. The spectra were normalized for the largest intensity peak and contain an offset to enhance readability.

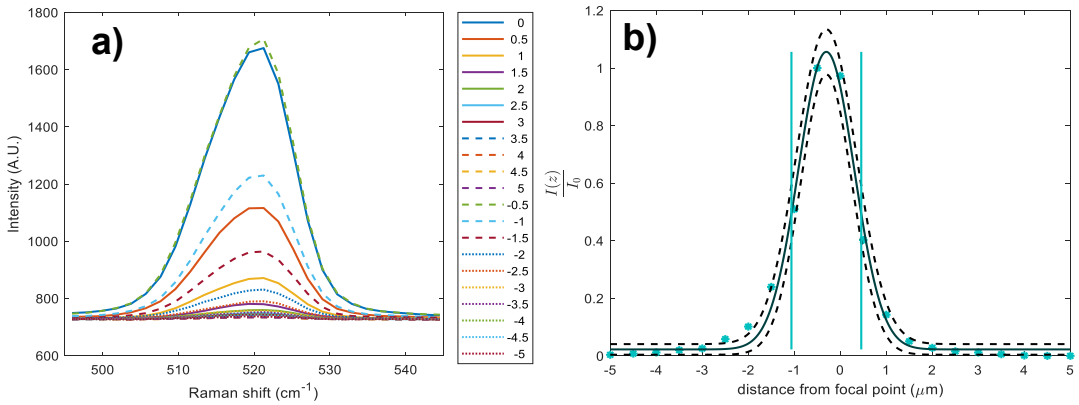

Figure S15 Recorded spectra for a 633 nm excitation laser wavelength at 100x magnification and 0.9 NA. The output laser power was 0.5 mW. a) The spectra were recorded on a flat silicon (001) substrate. b) shows the integrated normalized intensity (dotted) where a Gaussian fit was applied to determine normalized intensity distribution (solid line) with a 95% confidence interval (dashed line). The distance between the vertical lines indicates the calculated interaction length of the laser.[3]

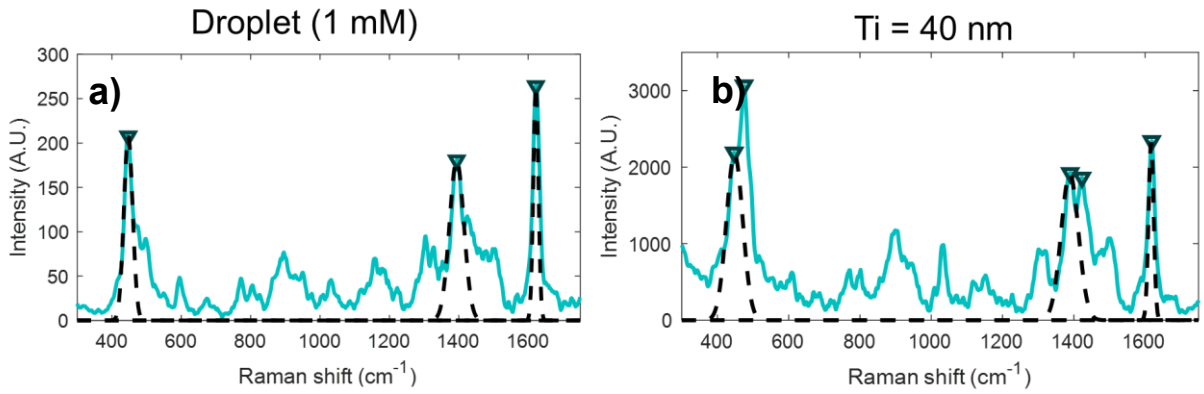

Figure S16. Examples of the peak detection algorithm (inverted triangle) and fitted Gaussian distribution (dashed line) for determination of I_{SERS} and I_{BULK} on recorded Raman spectra for a droplet a) and a substrate b). Note that there is a difference in vertical scaling for viewing purposes.

Table S3. The Raman band for MB solid and 1 mM of MB adsorbed over various Au-HNPs substrates. The excitation wavelength is 633 nm. Abbreviations: s, strong; w, weak; *ν*, stretching; *α*, in-plane ring deformation; *β*, in-plane bending; *γ*, out-of-plane bending; and *δ*, skeletal deformation. [4–6]

633 nm					
Solid MB (cm^{-1})	**Au flat (cm^{-1})**	**13 nm (cm^{-1})**	**20 nm (cm^{-1})**	**40 nm (cm^{-1})**	**Raman band**
444 (w)	446 (m)	448 (m)	446 (s)	448 (w)	*δ*(C-N-C)
	476 (m)	474 (s)	473 (s)	474 (w)	*δ*(C-N-C)
	894 (m)	903 (s)	896 (s)		*δ*(C–S–C)
		934 (s)	946 (s)		*β*(C–H)
	1034 (w)	1034 (s)	1031 (s)		*β*(C–H)
	1309 (w)	1302 (s)	1305 (s)		*α*(C–H)
1385 (w)	1394 (w)	1390 (s)	1387 (s)		*α*(C–H)
	1423 (m)	1423 (s)	1423 (s)	1424 (w)	ν_{asym}(C–N)
	1511 (m)	1489 (s)	1502 (s)	1510 (w)	ν_{asym}(C–C)
1617 (w)	1619(m)	1618 (s)	1619 (s)	1617 (w)	*ν*(C–C) ring
	1623 (w)	1623 (w)	1623 (w)	1623 (w)	*ν*(C–C) ring

Table S4. The Raman band for MB solid and 1 mM of MB adsorbed over various Au-HNPs substrates. The excitation wavelength is 785 nm. Abbreviations: s, strong; w, weak; *v*, stretching; *α*, in-plane ring deformation; *β*, in-plane bending; *γ*, out-of-plane bending; and *δ*, skeletal deformation.[7]

785 nm					
Solid MB (cm^{-1})	**Au flat (cm^{-1})**	**13 nm (cm^{-1})**	**20 nm (cm^{-1})**	**40 nm (cm^{-1})**	**Raman band**
437 (s)	439 (w)	441 (m)	439 (s)	439 (m)	*δ*(C-N-C)
482 (w)			467 (s)		*δ*(C-N-C)
			855 (s)		*β*(C–H)
		1031 (w)	1025 (s)		*β*(C–H)
			1011 (s)		
	1322 (w)		1309 (s)		*α*(C–H)
1382 (w)			1390 (s)	1390 (w)	*α*(C–H)
			1421 (s)	1421 (w)	ν_{asym}(C–N)
1609 (s)	1608 (w)		1609 (s)		*v*(C–C) ring
	1629 (w)	1629 (w)	1629 (w)	1629 (w)	*v*(C–C) ring

Supplemental files References

(1) Myers, R. H.; Montgomery, D. C.; Anderson-Cook, C. M. *Response Surface Methodology: Process and Product Optimization Using Designed Experiments*; Wiley Series in Probability and Statistics; Wiley, 2011.

(2) Montgomery, D. C.; Runger, G. C. *Applied Statistics and Probability for Engineers*, Sixth Edit.; John Wiley & Sons, Ltd., 2014.

(3) Le Ru, E. C.; Blackie, E.; Meyer, M.; Etchegoint, P. G. Surface Enhanced Raman Scattering Enhancement Factors: A Comprehensive Study. *J. Phys. Chem. C* **2007**, *111* (37), 13794–13803. https://doi.org/10.1021/jp0687908.

(4) Li, C.; Huang, Y.; Lai, K.; Rasco, B. A.; Fan, Y. Analysis of Trace Methylene Blue in Fish Muscles Using Ultra-Sensitive Surface-Enhanced Raman Spectroscopy. *Food Control* **2016**, *65*, 99–105. https://doi.org/10.1016/j.foodcont.2016.01.017.

(5) Santos, E. D. B.; Lima, E. C. N. L.; Oliveira, C. S. De; Sigoli, F. A.; Mazali, I. O. Fast Detection of Paracetamol on a Gold Nanoparticle-Chitosan Substrate by SERS. *Anal. Methods* **2014**, *6* (11), 3564–3568. https://doi.org/10.1039/c4ay00635f.

(6) Hou, M.; Huang, Y.; Ma, L.; Zhang, Z. Compositional Analysis of Ternary and Binary Chemical Mixtures by Surface-Enhanced Raman Scattering at Trace Levels. *Nanoscale Res. Lett.* **2015**, *10* (1), 1–7. https://doi.org/10.1186/s11671-015-1142-6.

(7) Xiao, G. N.; Man, S. Q. Surface-Enhanced Raman Scattering of Methylene Blue Adsorbed on Cap-Shaped Silver Nanoparticles. *Chem. Phys. Lett.* **2007**, *447* (4–6), 305–309. https://doi.org/10.1016/j.cplett.2007.09.045.